APL Materials

RESEARCH ARTICLE | JANUARY 23 2023

Structure–transport correlations in $Na_{11}Sn_2SbSe_{12}$ and its sulfide solid solutions

Special Collection: Challenges and Perspectives in Materials Chemistry—A Celebration of Prof. Sir Anthony K. Cheetham's 75th Birthday

Erika P. Ramos ; Abdeljalil Assoud ; Laidong Zhou ; Abhinandan Shyamsunder ; Daniel Rettenwander ; Linda F. Nazar

APL Mater. 11, 011104 (2023)
https://doi.org/10.1063/5.0129001

Structure–transport correlations in $Na_{11}Sn_2SbSe_{12}$ and its sulfide solid solutions

Cite as: APL Mater. 11, 011104 (2023); doi: 10.1063/5.0129001
Submitted: 2 October 2022 • Accepted: 30 December 2022 •
Published Online: 23 January 2023

Erika P. Ramos,[1,a] Abdeljalil Assoud,[1] Laidong Zhou,[1] Abhinandan Shyamsunder,[1] Daniel Rettenwander,[2,b] and Linda F. Nazar[1,c]

AFFILIATIONS

[1] Department of Chemistry and the Waterloo Institute for Nanotechnology, University of Waterloo, 200 University Ave. W, Waterloo, Ontario N2L 3G1, Canada
[2] Institute for Chemistry and Technology of Materials, Graz University of Technology (NAWI Graz), Stremayrgasse 9, 8010 Graz, Austria

Note: This paper is part of the Special Topic on Challenges and Perspectives in Materials Chemistry—A Celebration of Prof. Sir Anthony K. Cheetham's 75th Birthday.
[a] **Current address:** Materials Science Division, Lawrence Livermore National Laboratory, Livermore, California 94550, USA.
[b] **Current address:** Christian Doppler Laboratory for Solid-State Batteries and Department of Material Science and Engineering, NTNU Norwegian University of Science and Technology, Trondheim, Norway.
[c] **Author to whom correspondence should be addressed:** lfnazar@uwaterloo.ca

ABSTRACT

We report a new ion conductor—$Na_{11}Sn_2SbSe_{12}$—as a possible candidate for a solid catholyte in composite cathodes for all-solid state Na-batteries, which exhibits a room temperature ionic conductivity of 0.15 ± 0.03 mS cm^{-1} and an activation energy of 0.39 ± 0.02 eV. The sulfide solid solutions of $Na_{11}Sn_2SbSe_{12}$, namely, $Na_{11}Sn_2SbS_{12-x}Se_x$ (x = 1 and 6), were also investigated through a combination of Rietveld refinement against powder x-ray diffraction data and electrochemical impedance spectroscopy to reveal the complex structure–property relationships governing ion transport in this class of materials. Meanwhile, broadening of the Na-ion diffusion pathways in $Na_{11}Sn_2SbSe_{12}$ is expected to facilitate Na-ion transport compared to the sulfide-rich member of the solid solution, the opposite holds: increasing the Se fraction in $Na_{11}Sn_2SbS_{12-x}Se_x$ leads to a little change in the activation energy but a reduction in the ionic conductivity. We ascribe this to the lowering of the prefactor, σ_0, in the Arrhenius relationship with increasing lattice "softening" as a function of higher Se content.

I. INTRODUCTION

Li-ion batteries are currently the exclusive energy storage choice for many applications, such as electromobility. However, the cost of lithium is anticipated to increase over the next decade as the market share of EVs increases and other energy storage-dependent applications such as mini-grids, drones, and robots become more market-intensive. This is exacerbated by the fact that much of the untapped lithium reserves are located in remote or politically sensitive areas.[1–3] In addition, demand for cobalt, still a key component in Li-ion battery cathodes, and low producer inventories can create a bottleneck in the move toward improved energy storage systems.[2,4] Promising alternatives are Na-ion batteries (NIB). Sodium technology is considered to be a suitable choice in terms of battery cost, safety, and raw materials abundance.[1] Sodium is expected to be the next targeted element after lithium, based on its relatively low atomic weight, an electrochemical potential close to that of Li, and sustainability.[1,3,5] A multitude of "cobalt-free" positive electrode materials have been developed for NIB applications.[6–8] These cathodes include sulfur. Room-temperature Na–S batteries have prompted extensive research interest due to their high-charge storage capacity and abundance of both sodium and sulfur,[9,10] but the low electronic conductivity of sulfur (5×10^{-28} mS cm^{-1}) leads to very low utilization of the active material in the electrode as well as sluggish electrochemical reaction processes.[9] Elemental selenium, compared to sulfur, is regarded as an alternative promising cathode material for sodium (and lithium)-ion batteries[11,12] due to its considerably higher electrical conductivity (1 mS cm^{-1} for Se vs

0.5×10^{-24} mS cm^{-1} for S)[11] and a comparable volumetric capacity (3253 Ah l^{-1} based on a density of 4.82 g cm^{-3} vs 3467 Ah l^{-1} based on a density of 2.07 g cm^{-3}).[13,14] However, the organic liquid electrolytes used in Na-ion batteries have safety concerns due to their flammable nature and have cost factors that limit the realization of NIBs.[15–17] Solid-state NIBs with the integration of solid-state electrolytes (SEs) that form the basis for all-solid state batteries (ASSBs) are an alternative because they can potentially address these factors.[5,18,19] Na-ion SSEs, an essential component for realizing ASSBs, have been the subject of several studies that have led to the development of a wide range of new materials. Extensive development has been achieved in chalcogenide sodium-ion conductors;[20] for example, in 2015, the superionic conductor, cubic-Na_3PSe_4 (σ = 1.16 mS cm^{-1}), was synthesized by Zhang *et al.*,[18] followed by computational and experimental investigations of this material by Bo *et al.*[21] The crystal structure of the antimony analog, cubic-Na_3SbSe_4, was first identified in 1989,[22] although its ionic conductivity properties (σ = 3.7 mS cm^{-1}; E_a = 0.19 eV) were not measured until 2018. In both cubic-Na_3PSe_4 and cubic-Na_3SbSe_4 electrolytes, the enhancement of ion conductivity was observed compared to their sulfide-based counterparts that exhibit values of 0.2 and 2.8 mS cm^{-1}, respectively.[23,24] The opposite is true for the "NSPS" sulfide, $Na_{11}Sn_2PS_{12}$, whose ion conductivity was reported in the range of 3.7–2.5 mS cm^{-1}, respectively.[25,26] The synthesis of its antimony analog, $Na_{11}Sn_2SbS_{12}$, was reported at about the same time,[27] and the phospho-selenium analog, $Na_{11}Sn_2PSe_{12}$, was announced by two research groups who reported lower but similar ionic conductivities of 1.7[4] and 2.15 mS cm^{-1} at 25 °C.[28] The same selenide—prepared by a mechanochemical method—yielded an even slightly lower conductivity of 1 mS cm^{-1} after annealing, but, nonetheless, its very good performance as an electrolyte was demonstrated in Na–Se ASSBs.[29] The electrochemical performance of the selenium-poor antimonide $Na_{11}Sn_2SbS_{11.5}Se_{0.5}$ in ASSBs has also been reported; powder x-ray diffraction (PXRD) was utilized to identify compositions on the Se poor side (x < 0.8 in $Na_{11}Sn_2SbS_{12-x}Se_x$),[30] but the structure was not resolved by either powder or single-crystal methods, and structure–property relationships were not elucidated. Despite the increasing effort in developing Se-based solid electrolytes, the number of Na–Se ion conductors reported today is still limited, and compared to sulfides and oxides, selenides present a rather large field of discovery.

Here, we report that Se-substitution in $Na_{11}Sn_2SbS_{12}$ leads to the solid solution series $Na_{11}Sn_2SbS_{12-x}Se_x$ (x = 1, 6, and 12). The end member (x = 12) is a new Na-ion conductor (σ_i = 0.15 ± 0.03 mS cm^{-1}) with an activation energy of 0.39 ± 0.02 eV. Differential scanning calorimetry (DSC) measurements show that the material is stable to at least 500 °C. Our work encompasses structural characterization using both single-crystal and powder x-ray diffraction (PXRD), bond valence site energy (BVSE)[31,32] calculations to obtain the topology of ion-migration pathways in the framework, and electrochemical impedance spectroscopy. A combination of single-crystal x-ray diffraction and BVSE studies show that Na-ion conduction in $Na_{11}Sn_2SbSe_{12}$ relies on three-dimensional (3D) diffusion pathways in the framework involving the vast majority of the Na sites. As shown by single-crystal x-ray diffraction studies of $Na_{11}Sn_2SbS_{12-x}Se_x$ (x = 1, 6, and 12), the Se substitution enlarges the unit cell and increases Se^{2-} occupancy on the three *32g* Wyckoff positions, indicating the complete solubility of selenium in the framework. A decrease in ionic conductivity and an increase in activation energy with increasing Se content are observed in the chalcogenide solutions, $Na_{11}Sn_2SbS_{12-x}Se_x$ (x = 0 → 12). This contradicts expectations of higher conductivity based on a larger lattice volume, wider Na-ion channels, and a more polarizable anion framework but can be explained by consideration of the role of the prefactor in the Arrhenius relationship.

II. MATERIALS AND METHODS

A. Single-crystal synthesis of $Na_{11}Sn_2SbS_{12-x}Se_x$ (x = 1, 6, and 12)

$Na_{11}Sn_2SbS_{12-x}Se_x$ (x = 1, 6, and 12) were synthesized by combining Na_2S (99%, Sigma-Aldrich), Na_2Se (98%, Alfa Aesar), Na_2Se with Sb_2S_3 (99%, Sigma-Aldrich), S powder (99.9%, Sigma-Aldrich), Se powder (99%, Sigma-Aldrich), Sn powder (99%, Sigma-Aldrich), and Sb powder (99%, Sigma-Aldrich) in the targeted ratios. Na_2Se was prepared using elemental sodium and selenium with naphthalene as an electron transfer agent in tetrahydrofuran (THF) according to the procedure reported by Thompson and Boudjouk.[33] The precursors were combined according to the respective molar ratios of the targeted compositions and ball milled at 400 rpm for 33 h to yield the amorphous mixtures that were loaded into glassy carbon crucibles and vacuum sealed in quartz tubes. The mixtures were heated to 750 °C at a heating rate of 94 °C/h, held at this temperature for 5 h, and then slow-cooled over 79 h from 750 to 545 °C, followed by ice quenching. The resulting agglomerate of crystals was gently separated to pick suitable candidates for single-crystal x-ray diffraction studies.

B. Single crystal studies

Block-shaped, single crystals of $Na_{11}Sn_2SbS_{12-x}Se_x$ (x = 1, 6, and 12) with dimensions of 0.070 × 0.060 × 0.020; 0.160 × 0.110 × 0.040; and 0.130 × 0.090 × 0.030 mm^3, respectively, were obtained for crystal structure determination. X-ray diffraction data were collected at 280 K using a Bruker Kappa diffractometer equipped with a Smart Apex II CCD and graphite-monochromated Mo-Kα radiation. The single crystals were protected by a Paratone-N oil and liquid nitrogen flow using an Oxford Cryostream controller 700 at 280 K. Data were collected by scanning ω and ϕ with an increment of 0.3° in two groups of frames at different angles for complete data using the APEX II suite strategy. The exposure time was set to 30 s/frame. After unit cell indexation, the data were corrected for Lorentz and polarization effects, and multi-scan absorption corrections were applied using SADABS within the APEX II software suite. The structures were solved using the direct method, and all atoms were refined anisotropically by the least-squares fitting method incorporated in the SHELXTL package. The crystallographic structural details and bond distances are summarized in Tables I and S2–S10.

C. Powder diffraction and Rietveld refinements

X-ray diffraction measurements were performed on a PANalytical Empyrean instrument outfitted with a PIXcel bidimensional detector using Cu-Kα radiation. The microcrystalline powders were loaded into 0.3 mm capillaries in an argon-filled glovebox. Rietveld quality patterns were recorded in Debye–Scherrer geometry using

TABLE I. Atomic coordinates, occupation factor, and isotropic displacement parameters of $Na_{11}Sn_2SbSe_{12}$ obtained from single-crystal x-ray diffraction at 280 K.

Atom	Wyckoff site	x	y	z	SOF	U(eq) (Å^2)
Sn	*16e*	0.207 53(2)	1/2	1/4	1	0.019 00(6)
Sb	*8a*	0	1/4	3/8	1	0.018 27(7)
Se1	*32g*	0.107 99(2)	0.396 42(2)	0.199 25(2)	1	0.024 96(7)
Se2	*32g*	0.310 43(2)	0.403 68(2)	0.302 85(2)	1	0.021 82(7)
Se3	*32g*	0.090 94(2)	0.359 43(2)	0.424 74(2)	1	0.030 67(8)
Na1	*32g*	0.256 40(12)	0.271 57(11)	0.377 89(5)	0.926(6)	0.044 8(6)
Na2	*16d*	0	1/4	0.247 18(9)	0.869(8)	0.060 5(11)
Na3	*16e*	0.043 27(13)	1/2	1/4	0.962(7)	0.041 8(7)
Na4	*16c*	1/4	1/4	1/4	0.894(8)	0.055 6(10)
Na5	*16f*	0.227 92(10)	0.522 08(10)	3/8	0.969(8)	0.051 5(9)
Na6	*8b*	0	1/4	1/8	0.058(10)	0.020(11)

a parabolic x-ray mirror in the incident beam. Rietveld refinements for $Na_{11}Sn_2SbS_{12-x}Se_x$ (x = 1, 6, and 12) were performed using the models initially obtained from single-crystal XRD analysis. Rietveld refinements of each crystal structure were performed, where the scale factor, Chebyshev background, peak shape, and lattice parameters were simultaneously refined using the software package TOPAS 6 (Bruker-AXS). Refinement constraints that were used were as follows: the atomic coordinates and atomic displacement parameters were fixed to be the same as those obtained from the single crystal studies.

D. Conductivity measurements

AC impedance spectroscopy was initially performed on $Na_{11}Sn_2SbS_{12-x}Se_x$ solid solutions (x = 1, 6, and 12) using a VMP3 potentiostat/galvanostat (Bio-Logic Science Instruments) in the frequency range from 1 MHz to 0.1 Hz under 2–3 tons of constant pressure. The powders were cold pressed at 2 tons with stainless steel electrodes in a 10 mm diameter die to form pellets. The ionic conductivity was obtained using the equation $\sigma = t/RA$, where R is the total resistance of the solid electrolyte, t is the sample thickness (0.8 mm average), and A is the area of the solid electrolyte. The Nyquist plots of $Na_{11}Sn_2SbS_{12-x}Se_x$ (x = 1, 6, and 12) at room temperature were composed of one semicircle followed by a linear diffusion tail in the low-frequency region. The bulk and grain boundary contributions could not be deconvoluted, and therefore, the conductivities correspond to the total conductivity. The semicircle was fitted with a parallel circuit composed of a resistor (R) in parallel with a constant phase element (CPE) for the ionic transport, in series with a CPE that represents the blocking electrodes.[34,35] The temperature dependent ion conductivity measurements of $Na_{11}Sn_2SbS_{12-x}Se_x$ (x = 1, 6, and 12) were performed using the same custom-made Swagelok™ cell. The powders were pelletized at 2 metric tons of pressure, placed between two indium foils, and pressed at a lower pressure (~1 metric ton) to avoid indium being forced into the pellet and causing a short circuit. Impedance was measured at frequencies from 10 MHz to 0.3 Hz, every 5 °C, over a temperature range from 30 to 65 °C.

To separate the bulk conductivity of the grains from the grain boundaries in $Na_{11}Sn_2SbSe_{12}$, EIS was also conducted from 35 MHz to 1 Hz at temperatures from −100 to 100 °C every 10 °C. Data were recorded with a Novocontrol Concept 80 spectrometer that was connected to a Quatro cryo system and equipped with a zero-gradient synchrotron (ZGS) active sample cell (Novocontrol). Au thin films were sputter deposited with a thickness of 200 nm on both sides of the samples. The bulk conductivity of $Na_{11}Sn_2SbS_{12}$ was determined by fitting the data (Nyquist plots) over the range from −100 to −40 °C (Fig. S5). Each of the semicircles was fitted with a parallel circuit composed of a resistor (R) in parallel with a constant phase element (CPE) for the ionic transport, in series with a CPE that represents the blocking electrodes.

DC polarization measurements $Na_{11}Sn_2SbSe_{12}$ and c-$NaSbSe_2$ were performed by placing pellets between two stainless steel rods of 10 mm diameter and pressing them at 2 metric tons. Applied voltages of 0.25, 0.50, and 0.75 V for 30 min each were used. The experimental density of $Na_{11}Sn_2SbSe_{12}$ was 98.8% of the theoretical value. This value was calculated from the sample geometry and mass and compared to the theoretical density of 3.49 g/cm^3.

E. Bond valence site energy calculations

BVSE calculations were performed utilizing the SoftBV program with the bond valence parameter set developed by Chen and Adams.[36] The structural models obtained by single-crystal diffraction were used as an input. Na ion diffusion pathways were identified with the regions of low bond valence site energy for a dense grid of points with a resolution of 0.1 Å covering the crystal structure using the transferable Morse-type SoftBV forcefield. BVSE maps with an isosurface level of 0.4 eV over the global minimum are shown.

F. Differential scanning calorimetry

Between 5 and 10 mg of $Na_{11}Sn_2SbSe_{12}$ was placed in an aluminum pan and sealed under an argon atmosphere. Differential scanning calorimetry curves were obtained using a 10 °C/min heating and cooling rate up to 500 °C.

III. RESULTS AND DISCUSSION

A. Crystal structure of $Na_{11}Sn_2SbS_{12-x}Se_x$ (x = 1, 6, and 12)

The precursors for $Na_{11}Sn_2SbS_{12-x}Se_x$ (x = 1, 6, and 12) were mixed by mechanochemical ball-milling (see Sec. II). The PXRD

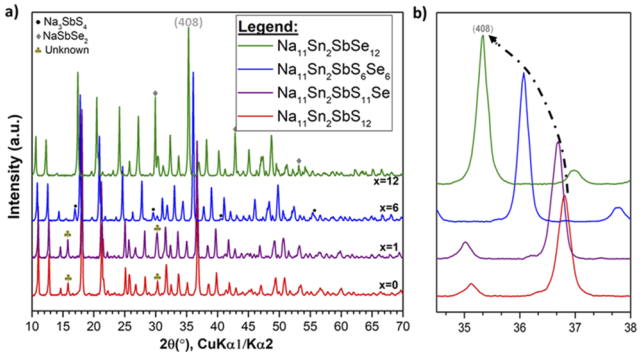

FIG. 1. (a) Room-temperature powder x-ray diffraction patterns of $Na_{11}Sn_2SbS_{12-x}Se_x$ (x = 0, 1, 6, and 12) with Na_3SbS_4, $NaSbSe_2$, and an unidentified impurity as labeled; (b) Expanded view on the right showing the peak shift in the (408) reflection toward the lower 2θ angle.

patterns of the as-milled precursors for $Na_{11}Sn_2SbS_{12-x}Se_x$ are shown in Fig. S1 (supplementary material). Halo patterns with no crystalline reflections that could be assigned to the starting materials were observed. After the mechanochemical process, a heat treatment was then conducted on the amorphous precursor mixtures (see Sec. II) to crystallize the desired materials. Figure 1(a) presents the room temperature PXRD patterns of the heat-treated $Na_{11}Sn_2SbS_{12-x}Se_x$ (x = 1, 6, and 12) materials, with the pattern of our previously reported $Na_{11}Sn_2SbS_{12}$ (x = 0)[27] shown for comparison. As illustrated in Fig. 1(b), owing to the larger ionic radius of Se vs S (1.98 vs 1.84 Å), as the Se content increases, the Bragg reflections, i.e., (408), show a shift toward higher *d*-spacing relative to $Na_{11}Sn_2SbS_{12}$, indicating the successful synthesis of a chalcogenide solid solution. Different impurity phases are observed throughout the $Na_{11}Sn_2SbS_{12-x}Se_x$ solid solution (Table S1); secondary-phase formation of Na_3SbS_4 and $NaSbSe_2$ are identified for x = 6 and x = 12, respectively, while a small unidentified impurity was formed for x = 1 (also observed in x = 0). The addition of small amounts of excess selenium (1 wt. %) was implemented in $Na_{11}Sn_2SbSe_{12}$ to compensate for any sodium loss during synthesis (750 °C) and reduce the secondary phase formation of $NaSbSe_2$ (Table S1), although the PXRD pattern still reveals its formation as a minority phase. Differential scanning calorimetry (DSC) was used to investigate the thermal stability of the $Na_{11}Sn_2SbSe_{12}$ end member. The DSC curve of $Na_{11}Sn_2SbSe_{12}$ (Fig. S2) shows no other significant contributions but only very minor signals at 176 and 318 °C, indicating that $Na_{11}Sn_2SbSe_{12}$ is stable up to 500 °C.

The opportunity to establish a detailed structural understanding of the solid solution series relies on the successful growth of single crystals of appropriate size and quality for single-crystal XRD studies. These were obtained for all three compositions (see Sec. II). Based on the single-crystal data (Tables I and S2–S10), we find the crystal structures of $Na_{11}Sn_2SbS_{12-x}Se_x$ (x = 1, 6, and 12) are isostructural to $Na_{11}Sn_2SbS_{12}$ and were solved in the same tetragonal space group $I4_1/acd$ (no. 142) Z = 8. A comparison of the unit cell parameters of $Na_{11}Sn_2SbS_{12-x}Se_x$ materials is presented in Fig. 2. The linear expansion of the unit cell volume from 5236 $Å^3$ for x = 0 to 5933 $Å^3$ for x = 12, with increasing Se content (+13% volume increase) stems from a significant increase in the lattice parameters (+4.3% in *a* and +4.1% in *c*), in accordance with the results obtained from powder XRD.

Figure 3(a) shows a representative powder x-ray diffraction pattern and Rietveld refinement against the x-ray data for $Na_{11}Sn_2SbSe_{12}$. The refinements for $Na_{11}Sn_2SbS_{12-x}Se_x$ (x = 1, 6, and 12) materials confirmed the formation of the targeted phases together with different impurity phases (Fig. S3). For x = 6, 4.75 wt. % of Na_3SbS_4 is present, while for x = 12, 12.5 wt. % of $NaSbSe_2$ is observed. An estimate of the amorphous content in x = 12 (~17%) was obtained by fitting the total area of the pattern (accounting for both crystalline and amorphous contributions) using Topas™ [Eq. (S1)], although this represents an overestimate since the glass capillary contributes to the background at ~20° and 50° in 2θ. Figure 3(b) displays the crystal structure of $Na_{11}Sn_2SbSe_{12}$ along the [100] and [001] directions. The structure of $Na_{11}Sn_2SbS_{12-x}Se_x$ encompasses two Wyckoff positions, *8a* and *16e*, for the polyhedral anions $[Sb(Q)_4]^{3-}$ and $[Sn(Q)_4]^{4-}$ (Q = S/Se), respectively. As expected, the volume of these polyhedra increased with the degree of selenium substitution (Fig. S4). Na-ions are distributed over six distinct crystallographic sites, five of which are octahedrally coordinated by chalcogenide ions and connected through face-sharing, while the "interstitial" Na(6) (*8b* Wyckoff position) site is loosely bonded to eight anions forming a quasi-cubic environment as previously described for $Na_{11}Sn_2SbS_{12}$.[27]

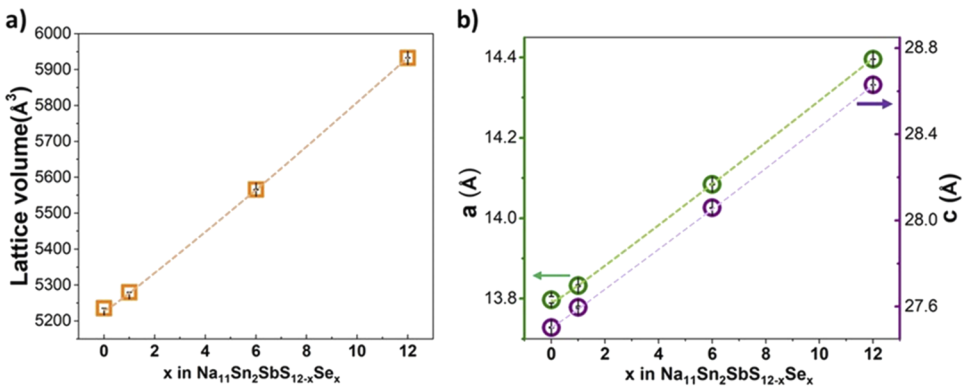

FIG. 2. Unit cell parameters of $Na_{11}Sn_2SbS_{12-x}Se_x$ with x = 0, 1, 6, and 12 obtained from single x-ray diffraction data at 280 K: (a) volume; (b) lattice parameters *a* and *c*.

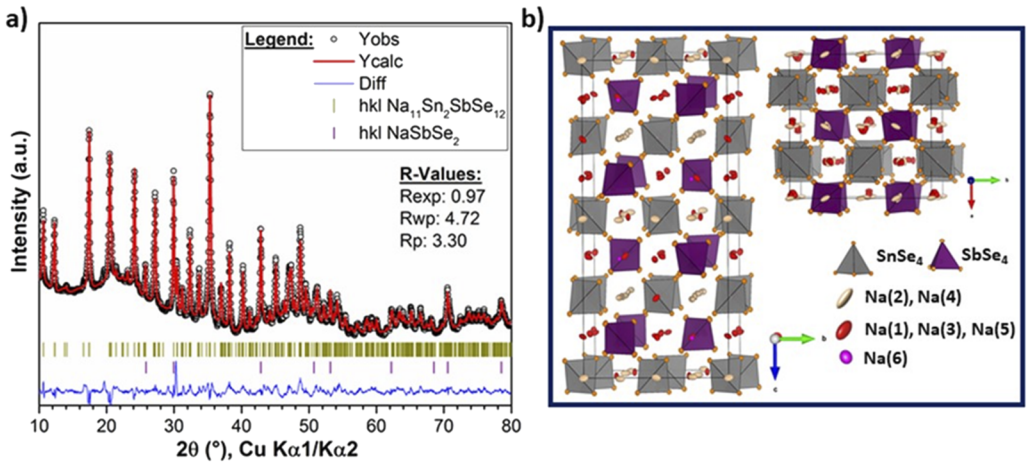

FIG. 3. Rietveld refinements of XRD data of (a) $Na_{11}Sn_2SbSe_{12}$. $NaSbSe_2$ is present as a minor secondary phase (12.5 wt. %). The black circles correspond to the data points, the red line denotes the calculated pattern, and the difference map is shown in blue. Olive vertical ticks correspond to Bragg reflections. (b) View of the structure of $Na_{11}Sn_2SbSe_{12}$ along the [100] and [001] directions. Thermal ellipsoids are drawn at 50% probability. Color code: Partially vacant sites Na(2) and Na(4): light-rose; almost fully occupied sites Na(1), Na(3), and Na(5): red; low occupied site Na(6): pink; Sn: gray; Sb: purple; Se: orange; $SnSe_4$ and $SbSe_4$ polyhedral are shown in gray and purple, respectively.

Representative single-crystal data for $Na_{11}Sn_2SbSe_{12}$ is shown in Table I. The Na content was refined to 11.15(6), slightly higher than the targeted stoichiometry but the same as reported for the x = 0 composition.[27] The effect of any additional minor sodium content on the conductivity is expected to be negligible, as shown by first principle studies.[37] Two of the five sodium sites are almost, but not quite, fully occupied [Na(3), site occupancy factor: SOF = 0.96 and Na(5), SOF = 0.97], and three sites are partially vacant [Na(1), SOF = 0.93; Na(2), SOF = 0.87; and Na(4), SOF = 0.89]. The sixth site is almost unoccupied [Na(6), SOF = 0.058]. In $Na_{11}Sn_2SbS_{12-x}Se_x$ (x = 1, 6, and 12), as expected and confirmed by bond length data (Tables S5, S8, and S10), the Na–Q bond length increases as the Se content increases (from 2.70 Å in x = 1 to 2.92 Å in x = 12), while all the Na^+–Na^+ interatomic distances are in the range of 3.5–3.67 Å in x = 12, resulting in equidistant Na-ion transport through the framework. Additional structural features, such as the increase of Se^{2-} occupancy on the three *32g* Wyckoff positions as the Se content increases in $Na_{11}Sn_2SbS_{12-x}Se_x$, were observed (Tables I, S3, and S6 and Fig. S4). The overall change in the Se occupancy on all three lattice sites suggests no site preference for Se.

Based on the single-crystal diffraction data of $Na_{11}Sn_2SbS_{12-x}Se_x$ materials, all five sodium sites [Na(1)–Na(5)] have an occupancy higher than 80%, while the probability that a sodium ion occupies the Na(6) site is rather low (SOF <14%) (Tables I, S3, and S6). The Na(6) site is a higher-energy site that is mostly vacant. Our previous work[38] and that of Oh *et al.*[37] unequivocally rule out Na-ion diffusion through the Na(6) site as an important pathway for Na-ion conduction. The diffusion channels created by face-sharing Na octahedra in the $Na_{11}Sn_2SbSe_{12}$ framework form a strategic alternating "full\vacancy\full" arrangement created by the partially vacant sodium sites at the cross-over points [32g (Na(1)) ~SOF = 93%; 16d (Na(2)) ~SOF = 87%; 16c (Na(4)) ~SOF = 89%] alternating with the almost fully occupied sodium sites [16e (Na(3))] and 16f (Na(5)) that spans in all three crystallographic directions (Table I). This alternating arrangement is essentially the same as in the sulfide $Na_{11}Sn_2SbS_{12}$ (and its P analog).[25,27] There is a slightly higher occupancy of the cross-over sites compared to $Na_{11}Sn_2SbS_{12}$ [Na(1) ~SOF = 89% and Na(2) ~SOF = 84%] that may affect transport, but to a very minor degree.

B. Ionic conduction properties of $Na_{11}Sn_2SbS_{12-x}Se_x$ (x = 1, 6, and 12)

The long-range Na-ion transport properties of $Na_{11}Sn_2SbS_{12-x}Se_x$ materials were examined by using the conventional complex impedance formalism (Table S11). A comparison between the ionic conductivities and activation energies obtained from EIS data for $Na_{11}Sn_2SbS_{12-x}Se_x$ (x = 1, 6, and 12) is shown in Figs. 4(a) and 4(b). The error in the obtained conductivities was determined from the span in the measurements of various samples of the same composition, and the values of the impedance analyses are presented in Table S12. The room temperature ionic conductivity decreases from 0.56 mS cm^{-1} for $Na_{11}Sn_2SbS_{12}$[27] to 0.34(2) mS cm^{-1} for $Na_{11}Sn_2SbS_{11}Se$ and to 0.15(3) mS cm^{-1} for $Na_{11}Sn_2SbSe_{12}$, while the activation energy increases only slightly within error from 0.34[27] to 0.37(2) and 0.39(2) eV, respectively [Figs. 5(a), 5(b), and S5]. Meanwhile, the total ionic conductivity of $Na_{11}Sn_2SbSe_{12}$ may be slightly impacted by the minority phase $NaSbSe_2$ (~12 wt. %, Table S1), the overall trend in lower conductivity with increasing Se content suggests this is mainly governed by the bulk properties of the materials. This conclusion is especially true from x = 0 → 6, where the impurity fraction is only in the region of 4%–5%. The higher occupancy of the cross-over points, as mentioned above, may impact fast ion conduction by lowering the frequency of cooperative Na-ion hopping both in the *ab* plane and along the *c* axis.

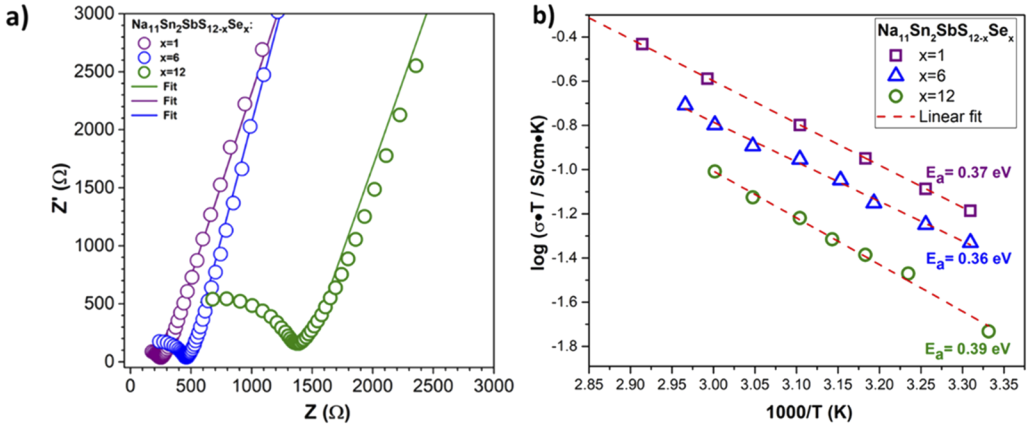

FIG. 4. (a) Room temperature Nyquist impedance plot of $Na_{11}Sn_2SbS_{12-x}Se_x$ (x = 1, 6, and 12) with the respective equivalent circuit shown. The fitted data are presented in Table S11; (b) Arrhenius plot of the total conductivity of $Na_{11}Sn_2SbS_{12-x}Se_x$ (x = 1, 6, and 12) from 30 to 65 °C.

As expected, Se substitution gives rise to an increase in the unit cell lattice parameters and hence the unit cell volume [5236 $Å^3$ for S vs 5933 $Å^3$ for Se, Fig. 2(a)], which should favor Na-ion diffusion. However, the decrease in ionic conductivity and increase in activation energy as the Se content increases contradict expectations based on the larger lattice volume and more polarizable anion framework of $Na_{11}Sn_2SbSe_{12}$. The Se^{-2} substitution in $Na_{11}Sn_2SbS_{12-x}Se_x$ makes the lattice softer, i.e., creating longer/weaker bonds (Fig. S6) affecting all cation–anion interactions, but leads to an unexpected trend in increasing activation energy with a more polarizable anion framework. We note that lower ion conductivity for Se vs S analog is not without precedent; for example, as mentioned in the introduction, $Na_{11}Sn_2PS_{12}$ exhibits an ion conductivity between 3.7 and 2.5 mS cm^{-1},[25,26] whereas the phospho-selenium analog, $Na_{11}Sn_2PSe_{12}$, displays lower ionic conductivities between 1.7 and 2.15 mS cm^{-1}.[4,28]

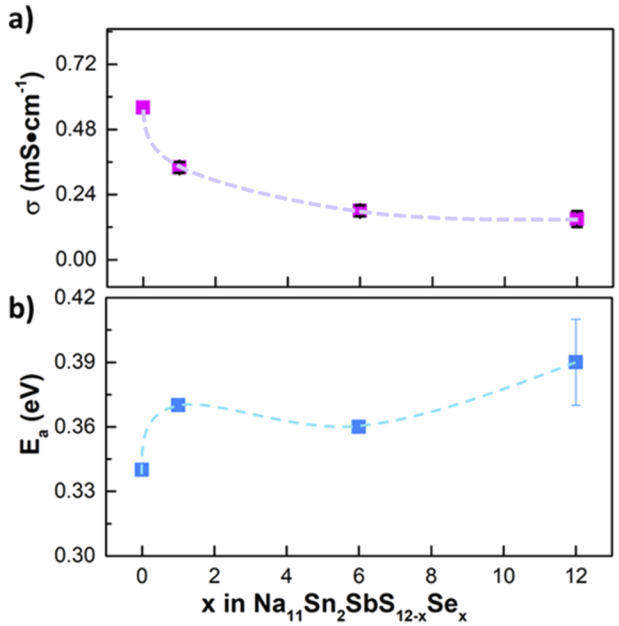

FIG. 5. Data for $Na_{11}Sn_2SbS_{12-x}Se_x$ (x = 0, 1, 6, and 12). (a) Ionic conductivity as a function of Se content; (b) activation energy, E_a. The data for $Na_{11}Sn_2SbS_{12}$ were taken from Ref. 27. The dotted lines are shown for guidance to the eye.

A report on argyrodites Li_6PS_5X (X = Cl, Br, I)[39] reveals the contradictory contributions to the conductivity from the Arrhenius prefactor and E_a, namely, that as the lattice polarizability increases, E_a often decreases due to softening of the lattice, but the prefactor σ_0 also decreases owing to a decrease in the jump frequency. That leads to an overall decrease in conductivity with the increasing softness of the anion lattice in the argyrodites. For the $Na_{11}Sn_2SbS_{12-x}Se_x$ solid solution, a relatively small change in E_a is observed on the Se substitution (from 0.34 eV for x = 0 to 0.39 eV for x = 12), suggesting that the drop in the prefactor (see Fig. 4)—as dictated by the higher polarizability of $Se^{\delta-}$ compared with $S^{\delta-}$—likely governs the ionic conductivities of $Na_{11}Sn_2SbS_{12-x}Se_x$. This may also explain the lower conductivity of $Na_{11}Sn_2PSe_{12}$ vs $Na_{11}Sn_2PS_{12}$ (see above). Further studies will be conducted to deconvolute the influence of lattice vibrations (softening of the lattice) on ionic transport, but these are beyond the current scope of the work.

The BVSE approach was used to explore the potential ion migration pathways in $Na_{11}Sn_2SbSe_{12}$. Figures 6(a)–6(c) display the bond valence model of Na-ion migration pathways in $Na_{11}Sn_2SbSe_{12}$ along the *a*,*b*-plane and *c*-axis, respectively, with the structure in the polyhedral motif shown for comparison [Figs. 6(b)–6(d)]. The BVSE maps, depicted as isosurfaces of constant bond valence site energy, suggest 3D interconnected network pathways that are displayed as yellow isosurfaces. These involve all the Na sites that form the major conduction pathways in the framework, for example, Na(4)-Na(2)-Na(4) and Na(2)-Na(3)-Na(2) chains along the *a*,*b*-plane [Fig. 6(b)] and Na(4)-Na(1)-Na(3)-Na(1)-Na(4) chains along the *c*-axis [Fig. 6(d)].

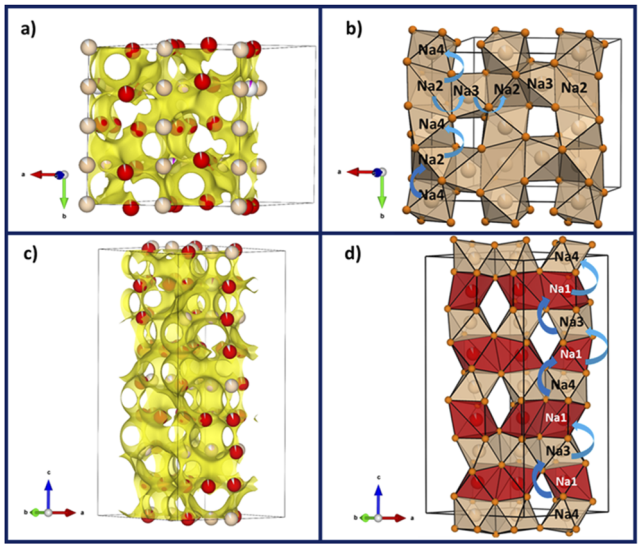

FIG. 6. (a) Bond valence map model of Na-ion migration pathways in $Na_{11}Sn_2SbSe_{12}$ visualized as isosurfaces of constant bond valence site energy in the *ab* plane; (b) View of the diffusion channels interconnecting Na(4)–Na(2)–Na(4) and Na(2)–Na(3)–Na(2) along the *ab* plane; (c) Bond valence map model of Na-ion migration pathways visualized as isosurfaces along the *c* axis; (d) View of the diffusion channels interconnecting Na(4)–Na(1)–Na(3)–Na(4) sites along the *c* axis. Color code: Na(2), Na(3), and Na(4): light rose; Na(1): red.

The room temperature electronic conductivity of $Na_{11}Sn_2SbSe_{12}$ was measured by the DC polarization of the SS/$Na_{11}Sn_2SbSe_{12}$/SS symmetric cell. Figure S7(a) shows the DC polarization curves at three different voltages: 0.25, 0.50, and 0.75 V. The small potential applied to $Na_{11}Sn_2SbSe_{12}$ between the two SS blocking electrodes leads to a decrease in the current until a steady-state value is reached. From a linear fit of voltage vs stabilized current [Fig. S7(b)], the electronic conductivity for $Na_{11}Sn_2SbSe_{12}$ was estimated to be $4.9 \pm 0.6 \times 10^{-4}$ mS cm^{-1}, which is three orders of magnitude lower than the ionic conductivity (1.5×10^{-1} mS cm^{-1}). The secondary-phase c-$NaSbSe_2$ should not contribute to the overall electronic conductivity as σ_e is similar (2×10^{-3} mS cm^{-1}; Fig. S8), and its low mass fraction will not result in discrete percolation pathways. Meanwhile the propensity of $Na_{11}Sn_2SbSe_{12}$ to reduction at a sodium electrode would obviate the application of $Na_{11}Sn_2SbSe_{12}$ as a separator, the other properties of this 3D Na-ion conductor (fast Na-ion transport and a thermally stable structure) make it a potential candidate as a SE in composite cathode materials for ASSB applications.

IV. CONCLUSIONS

In this work, Se^{2-} substitution in $Na_{11}Sn_2SbS_{12-x}Se_x$ x = 1, 6, and 12 led to the synthesis of the new Na-ion conductor, $Na_{11}Sn_2SbSe_{12}$, with a room temperature ionic conductivity of 0.15 mS cm^{-1} and an activation energy of 0.39 eV. Based on the single-crystal diffraction studies performed on $Na_{11}Sn_2SbS_{12-x}Se_x$ (x = 1, 6, and 12), we find that with increasing Se^{2-} substitution, a uniform increase in lattice parameters and occupancy of the three *32g* Wyckoff positions by Se^{2-} was observed. Bond valence energy site calculation results show that the $Na_{11}Sn_2SbSe_{12}$ framework is comprised of a 3D interconnected network likely involving all Na sites forming the major conduction pathways, as previously reported for the sulfide analog. Meanwhile the increase of the Na channel volume with Se^{2-} substitution should be more beneficial for Na-ion transport, increasing the Se fraction in $Na_{11}Sn_2SbS_{12-x}Se_x$ leads to an increase in the activation energy (0.34 eV for x = 0 to 0.39 eV for x = 12) and a reduction in the ionic conductivity (0.56 mS cm^{-1} for x = 0 to 0.15 mS cm^{-1} for x = 12). The higher occupancy of the cross-over point [Na(1) with a SOF of 93%] may impact the ion conduction by lowering the prospect of cooperative 3D Na-ion diffusion, but this is not expected to be a major contribution. We note that such "anomalous" behavior has been previously reported, as the conductivity of $Na_{11}Sn_2PS_{12}$ (3.7–2.5 mS cm^{-1}) is higher than that of its Se analog, $Na_{11}Sn_2PSe_{12}$ (1.7–2.15 mS cm^{-1}). We attribute this to the fact that a decrease in the prefactor, σ_0, owing to a softer anion lattice, may govern the decrease in conductivity when E_a remains fairly constant. Further studies need to be conducted to deconvolute the influence of lattice vibrations (softening of the lattice) on ionic transport. Nonetheless, these detailed structural solutions of the solid solution series—$Na_{11}Sn_2SbS_{12-x}Se_x$—provide a better understanding of the transport properties of this structure type.

SUPPLEMENTARY MATERIAL

See the supplementary material for additional information on the crystallography and electrochemistry data.

ACKNOWLEDGMENTS

L.F.N. acknowledges the NSERC for financial support of this work through their Discovery and Canada Research Chair programs and partial support from the Joint Center for Energy Storage Research, an Energy Innovation Hub funded by the U.S. Department of Energy (DOE), Office of Science, Basic Energy Sciences. E.P.R. thanks Lawrence Livermore National Laboratory for their support via the career development program. D.R. acknowledges financial support from the Austrian Federal Ministry for Digital and Economic Affairs, the National Foundation for Research, Technology and Development, and the Christian Doppler Research Association (Christian Doppler Laboratory for Solid-State Batteries).

AUTHOR DECLARATIONS

Conflict of Interest

The authors have no conflicts to disclose.

Author Contributions

Erika P. Ramos: Conceptualization (equal); Formal analysis (lead); Investigation (lead); Writing – original draft (lead); Writing – review & editing (equal). **Abdeljalil Assoud**: Investigation (equal); Methodology (equal). **Laidong Zhou**: Investigation (equal); Validation (equal). **Abhinandan Shyamsunder**: Investigation (equal). **Daniel**

Rettenwander: Investigation (equal). **Linda F. Nazar**: Conceptualization (equal); Funding acquisition (lead); Supervision (lead); Writing – review & editing (lead).

DATA AVAILABILITY

The data that support the findings of this study are available within the article and its supplementary material.

REFERENCES

[1] V. Palomares, P. Serras, I. Villaluenga, K. B. Hueso, J. Carretero-González, and T. Rojo, Energy Environ. Sci. **5**, 5884 (2012).
[2] M. Li, J. Lu, Z. Chen, and K. Amine, Adv. Mater. **30**, 1800561 (2018).
[3] J.-J. Kim, K. Yoon, I. Park, and K. Kang, Small Methods **1**, 1700219 (2017).
[4] M. Duchardt, S. Neuberger, U. Ruschewitz, T. Krauskopf, W. G. Zeier, J. Schmedt auf der Günne, S. Adams, B. Roling, and S. Dehnen, Chem. Mater. **30**, 4134 (2018).
[5] Z. Yu, L. Shang, J. Hwan Seo, D. Wang, X. Luo, Q. Huang, S. Chen, J. Lu, X. Li, Z. Kui Liu, and D. Wang, Adv. Mater. **29**, 1605561 (2017).
[6] Juliette Billaud, J. Raphaele Clément, A. Robert Armstrong, Jesus Canales-Vázquez, Patrick Rozier, Clare P. Grey, and Peter G. Bruce, J. Am. Chem. Soc. **136**, 17243 (2014).
[7] N. Yabuuchi, M. Kajiyama, J. Iwatate, H. Nishikawa, S. Hitomi, R. Okuyama, R. Usui, Y. Yamada, and S. Komaba, Nat. Mater. **11**, 512 (2012).
[8] J. R. Kim and G. G. Amatucci, J. Electrochem. Soc. **163**, A696 (2016).
[9] H. Wang, Y. Jiang, and A. Manthiram, Adv. Energy Mater. **8**, 1701953 (2018).
[10] S. Xin, Y.-X. Yin, Y.-G. Guo, and L.-J. Wan, Adv. Mater. **26**, 1261 (2014).
[11] J. Ding, H. Zhou, H. Zhang, T. Stephenson, Z. Li, D. Karpuzov, and D. Mitlin, Energy Environ. Sci. **10**, 153 (2017).
[12] X. Li, J. Liang, J. Luo, C. Wang, X. Li, Q. Sun, R. Li, L. Zhang, R. Yang, S. Lu, H. Huang, and X. Sun, Adv. Mater. **31**, 1808100 (2019).
[13] C. Luo, Y. Xu, Y. Zhu, Y. Liu, S. Zheng, Y. Liu, A. Langrock, and C. Wang, ACS Nano **7**, 8003 (2013).
[14] L. Wang, X. Zhang, L. Deng, J. Tang, H. Deng, W. Hu, and Z. Liu, ACS Appl. Mater. Interfaces **11**, 4995 (2019).
[15] C. Sun, J. Liu, Y. Gong, D. P. Wilkinson, and J. Zhang, Nano Energy **33**, 363 (2017).
[16] S. Xin, Y. You, S. Wang, H.-C. Gao, Y.-X. Yin, and Y.-G. Guo, ACS Energy Lett. **2**, 1385 (2017).
[17] C. Zhou, S. Bag, and V. Thangadurai, ACS Energy Lett. **3**, 2181 (2018).
[18] L. Zhang, K. Yang, J. Mi, L. Lu, L. Zhao, L. Wang, Y. Li, and H. Zeng, Adv. Energy Mater. **5**, 1501294 (2015).
[19] L. Zhang, D. Zhang, K. Yang, X. Yan, L. Wang, J. Mi, B. Xu, and Y. Li, Adv. Sci. **3**, 1600089 (2016).
[20] J. W. Heo, A. Banerjee, K. H. Park, Y. S. Jung, and S.-T. Hong, Adv. Energy Mater. **8**, 1702716 (2018).
[21] S.-H. Bo, Y. Wang, J. C. Kim, W. D. Richards, and G. Ceder, Chem. Mater. **28**, 252 (2016).
[22] Brigitte Eisenmann and Roland Zagler, Z. Naturforsch. **44b**, 249–256 (1989).
[23] A. Hayashi, K. Noi, A. Sakuda, and M. Tatsumisago, Nat. Commun. **3**, 856 (2012).
[24] D. Zhang, X. Cao, D. Xu, N. Wang, C. Yu, W. Hu, X. Yan, J. Mi, B. Wen, L. Wang, and L. Zhang, Electrochim. Acta **259**, 100 (2018).
[25] Z. Zhang, E. Ramos, F. Lalère, A. Assoud, K. Kaup, P. Hartman, and L. F. Nazar, Energy Environ. Sci. **11**, 87 (2017).
[26] M. Duchardt, U. Ruschewitz, S. Adams, S. Dehnen, and B. Roling, Angew. Chem., Int. Ed. **57**, 1351 (2018).
[27] E. P. Ramos, Z. Zhang, A. Assoud, K. Kaup, F. Lalère, and L. F. Nazar, Chem. Mater. **30**, 7413 (2018).
[28] Z. Yu, S.-L. Shang, D. Wang, Y. C. Li, H. P. Yennawar, G. Li, H.-T. Huang, Y. Gao, T. E. Mallouk, Z.-K. Liu, and D. Wang, Energy Storage Mater. **17**, 70 (2019).
[29] R. P. Rao, X. Zhang, K. C. Phuah, and S. Adams, J. Mater. Chem. A **7**, 20790 (2019).
[30] H. Wan, L. Cai, W. Weng, J. P. Mwizerwa, J. Yang, and X. Yao, J. Power Sources **449**, 227515 (2020).
[31] S. Adams and R. P. Rao, in *Bond Valences*, edited by I. D. Brown and K. R. Poeppelmeier (Springer, Berlin, Heidelberg, 2014), pp. 129–159.
[32] S. Adams and R. P. Rao, Phys. Status Solidi A **208**, 1746 (2011).
[33] D. P. Thompson and P. Boudjouk, J. Org. Chem. **53**, 2109 (1988).
[34] P. Vadhva, J. Hu, M. J. Johnson, R. Stocker, M. Braglia, D. J. L. Brett, and A. J. E. Rettie, ChemElectroChem **8**, 1930 (2021).
[35] V. Vivier and M. E. Orazem, Chem. Rev. **122**, 11131 (2022).
[36] H. Chen and S. Adams, IUCrJ **4**, 614 (2017).
[37] K. Oh, D. Chang, I. Park, K. Yoon, and K. Kang, Chem. Mater. **31**, 6066 (2019).
[38] Z. Zhang, P.-N. Roy, H. Li, M. Avdeev, and L. F. Nazar, J. Am. Chem. Soc. **141**, 19360 (2019).
[39] M. A. Kraft, S. P. Culver, M. Calderon, F. Böcher, T. Krauskopf, A. Senyshyn, C. Dietrich, A. Zevalkink, J. Janek, and W. G. Zeier, J. Am. Chem. Soc. **139**, 10909 (2017).